Migration of the Antarctic Polar Front over the last glacial cycle

Lena Thöle
Department of Earth Sciences, Marine Palynology and Paleoceanography, Utrecht University, Utrecht

Xuyuan Ai (xuyuana@princeton.edu)
Princeton University https://orcid.org/0000-0003-1353-6114

Alexandra Auderset
Max Planck Institute for Chemistry https://orcid.org/0000-0002-6316-4980

Mareike Schmitt
Max Planck Institute for Chemistry

Simone Moretti
Max Planck Institute for Chemistry https://orcid.org/0000-0002-6772-7269

Anja Studer
Department of Environmental Sciences, University of Basel, Basel https://orcid.org/0000-0001-7354-8497

Elisabeth Michel
Laboratoire des Sciences du Climat et de l'Environnement, UMR CEA-CNRS-UVSQ 8212, Institut Pierre-Simon Laplace https://orcid.org/0000-0001-7810-8888

Martin Wegmann
University of Bern https://orcid.org/0000-0002-5294-2978

Alain Mazaud
Laboratoire des Sciences du Climat et de l'Environnement, LSCE/IPSL, CNRS-CEA-UVSQ, Université de Paris-Saclay, Gif-sur-Yvette

Peter Bijl
Faculty of Geosciences, Utrecht University https://orcid.org/0000-0002-1710-4012

Daniel Sigman
Princeton University https://orcid.org/0000-0002-7923-1973

Alfredo Martinez-Garcia
Max Planck Institute for Chemistry https://orcid.org/0000-0002-7206-5079

Samuel L. Jaccard
Institute of Earth Sciences, University of Lausanne

Article

Keywords: Paleoceanography, glacial–interglacial changes, Southern Ocean, ACC, atmospheric CO2

Posted Date: March 8th, 2022

DOI: https://doi.org/10.21203/rs.3.rs-1364006/v1

Migration of the Antarctic Polar Front over the last glacial cycle

Lena M. Thöle[1, 2, 3†*], Xuyuan E. Ai[2, 4†*], Alexandra Auderset[2], Mareike Schmitt[2], Simone Moretti[2], Anja S. Studer[2, 5], Elisabeth Michel[6], Martin Wegmann[7], Alain Mazaud[6], Peter K. Bijl[3], Daniel M. Sigman[4], Alfredo Martínez-García[2], Samuel L. Jaccard[1,8*]

[1]Institute of Geological Sciences and Oeschger Centre for Climate Change Research, University of Bern, Bern, Switzerland.

[2]Max Planck Institute for Chemistry, Climate Geochemistry Department, Mainz, Germany.

[3]Marine Palynology and Paleoceanography, Department of Earth Sciences, Utrecht University, The Netherlands.

[4]Department of Geosciences, Princeton University, Princeton, NJ, USA.

[5]Aquatic and Isotope Biogeochemistry, Department of Environmental Sciences, University of Basel, Switzerland.

[6]Laboratoire de Sciences et de l'Environnement (LSCE), Gif-sur-Yvette, France.

[7]Institute of Geography and Oeschger Centre for Climate Change Research, University of Bern, Bern, Switzerland.

[8]Institute of Earth Sciences, University of Lausanne, Lausanne, Switzerland.

[†]Contributed equally to this work

[*]Corresponding authors: Lena M. Thöle (l.m.thole@uu.nl), Xuyuan E. Ai (xuyuana@princeton.edu), and Samuel L. Jaccard (Samuel.jaccard@unil.ch)

Key points

Paleoceanography, glacial–interglacial changes, Southern Ocean, ACC, atmospheric CO_2

Word counts

Abstract: 153, Main: 4428, Methods: 1905

Abstract

The Southern Hemisphere Westerly Winds (SWW) drive upwelling south of the Antarctic Polar Front (PF) that vents CO_2 to the atmosphere. During the ice ages, a northward (equatorward) shift of the PF may have reduced this CO_2 venting, helping to explain the lower atmospheric CO_2 concentration of those times. However, evidence of PF migration is lacking. Here, we report biomarker–based sea surface temperature (SST) reconstructions from two marine sediment cores at different latitudes in the Southern Indian Ocean across the last glacial cycle. Using a quantitative framework for the effect of the PF on meridional SST gradient, we show that the PF underwent an equatorward shift during the ice ages. The PF latitude reconstruction, when compared with other data, also suggests a role for Earth's axial tilt in the strength and latitude range of SWW-driven upwelling, which may explain previously noted deviations in atmospheric CO_2 from a simple correlation with Antarctic climate.

Introduction

Recent studies have estimated that, over the last 150 years, 40% of the global oceanic uptake of anthropogenic CO_2 has taken place in the Southern Ocean[1,2], and the region appears to account for an even larger fraction of excess heat uptake by the ocean[3,4]. Yet, it remains unclear how the Southern Ocean carbon and heat sinks will evolve in the face of continued anthropogenic climate change[5–7].

On glacial–interglacial timescales, it is believed that the Southern Ocean strongly impacts the atmospheric CO_2 inventory owing to its leverage on the communication between the atmosphere and the voluminous ocean carbon reservoir[8,9]. Several mechanisms are proposed to have curbed CO_2 release from the ocean interior during glacial periods, including sea ice expansion[10,11], an increase in Subantarctic phytoplankton productivity fueled by higher Fe-bearing dust supply to the surface ocean[12,13], and weaker exchange of surface waters with CO_2-rich deep water masses in the Antarctic Zone (AZ)[14–20].

Changes in the position and/or strength of Southern Hemisphere Westerly Winds (SWW) during glacial times are thought to have modulated Antarctic upwelling[21–23]. Surface winds indeed cause divergent Ekman transport south of the wind stress maximum, near the axis of the Antarctic Circumpolar Current (ACC) between 45-55°S, leading to the upwelling of CO_2- and nutrient-rich subsurface waters along tilted surfaces of constant density. These isopycnals run poleward and upward across the ACC[24], inducing strong meridional sea surface temperature (SST) and density gradients that define fronts[25]. The Polar Frontal Zone (PFZ) marks the transition from the cold Antarctic Zone to the south, where deep water masses outcrop, to the much warmer surface waters of the Subantarctic Zone (SAZ) to the north. The PFZ is defined by the Antarctic Polar Front (PF) to the south and the Subantarctic Front (SAF) to the north.

Analysis of modern oceanographic data and numerical simulations suggest that the PF is largely steered by seafloor bathymetry due to the deep structure of the frontal jets, but the extent of frontal shift under substantial climate forcing is still under debate[26–28]. Similarly, model simulations are not consistent in evaluating the effect of changing SWW stress on upwelling intensity[29,30]. On glacial–interglacial timescales, available paleoceanographic reconstructions qualitatively agree on the direction of latitudinal shifts of the ACC fronts[31–36] but do not agree on coherent temporal patterns of change in the SWW[37]. SST-based paleoceanographic evidence of front dynamics has been lacking. Previous radiolarian-based reconstructions of SST from the Atlantic sector of the AZ and SAZ suggest a 2-4° northward shift of the isotherms representative of the modern PF and SAF during the Last Glacial Maximum (LGM), which was interpreted to reflect a northward shift of the ACC[36]. A recent study investigated the surface and subsurface temperature changes in the Indian Southern Ocean; assuming one isotherm as representative of the PF, a more northward PF location is reconstructed for the LGM and a more poleward position for MIS 5e[33]. A concern with the single-isotherm method is that SST may change due to either changes in SST spatial gradients or global/hemispheric climate change. Compilation of planktic foraminiferal $\delta^{18}O$ across the Southern Ocean, after correction for whole-ocean change in sea water $\delta^{18}O$, also suggests an equatorward shift of the PF[38]. What would be more informative is the temporal evolution of the strong temperature gradient associated with the northern boundary of Antarctic surface, especially for investigating changes in Southern Ocean upwelling and its drivers[17,20,21,39].

To shed light on the timing and structure of ACC frontal movements and connect these with changes in SWW and upwelling dynamics, we present reconstructions of the gradient in the meridional SST field across the ACC. Using TEX^{L}_{86} paleothermometry[40–42], we analyze the temporal evolution of reconstructed SST in the southwest Indian Ocean close to the Kerguelen Plateau based on marine sediment cores MD11-3357 (44.68°S, 80.43°E, 3,349 m water depth) and MD11-3353 (50.57°S, 68.39°E, 1,568 m water depth) in the Subantarctic and Antarctic zones (SAZ and AZ) of the Southern Ocean, respectively (Fig. 1). The meridional SST difference (ΔSST) between the SAZ and AZ sites was used to investigate the temporal evolution of frontal displacements. In combination with a simple quantitative framework that relates front displacements to ΔSST, our analyses lend strong support to the hypothesis of PF migration during the last glacial cycle, with a generally more equatorward position during cold periods and more poleward location during warm intervals. We argue that the mean position of the SWW had a profound impact on the latitudinal position of the Southern Ocean fronts, while the position and intensity of the SWW together modulate Southern Ocean upwelling intensities and thus regulating glacial-interglacial atmospheric $p\mathrm{CO_2}$ changes.

Results and Discussions

SST changes and the link to frontal shifts

The youngest (core-top) samples from the SAZ (1,100 years ago) and AZ (1,200 years ago) sediment cores provide SST estimates of 13.1°C and 5.1°C, respectively (Fig. 2), 1.8°C and 0.5°C warmer than the modern summer SST[43] (11.3°C and 4.7°C, respectively), which lies within the error of the temperature calibration[42]. Both SST records are closely correlated with Antarctic ice core temperature reconstruction[44] (Fig. 2) and portray a coherent glacial-interglacial evolution consistent with other Southern Ocean SST reconstructions[45–47]. The records depict a glacial-interglacial SST amplitude of about 8°C (Fig. 2), in good agreement with multi-proxy SST reconstructions in the area[48–50]. Southern Ocean temperature estimates tend to record glacial-interglacial SST changes that are twice as large as global temperature reconstructions[51,52]. It has been argued that frontal shifts may help to explain the larger glacial-interglacial SST amplitude observed in the Southern Ocean[46]. Consistent with this interpretation, sites further away from the ACC experienced reduced SST changes of about 4°C[46].

The location of the modern PF has been inferred based on different metrics, such as the maximum meridional gradient in seawater properties[53,54] or the winter 2°C isotherm[25,55]. Here, we adhere to the maximum gradient in surface layer temperature, as it reflects the boundary between surface water masses originating from different sources (see Methods, Supplementary Fig. 5). In World Ocean Atlas 2018, the steepest slope of surface temperature in the Kerguelen region lies north of AZ site MD11-3353 and mostly south of SAZ site MD11-3357, resulting in an SST difference of 6.5°C between the two sites[43]. ΔSST would decrease and thus SSTs become more similar if — as a consequence of frontal shifts — both sites recorded temperatures from more similar water masses. This can result from either a northward or a southward shift of the front.

The reconstructed ΔSST between the SAZ and the AZ core sites during the past 150,000 years shows a pattern distinct from that of the glacial-interglacial climate evolution (Fig. 2). During peak glacial intervals such as MIS 2, MIS 4, and MIS 6, ΔSST is reduced to 4-6 °C. It reaches maximum values of >7 °C during intermediate climate intervals, such as MIS 5c and MIS 3, while during peak interglacials, ΔSST drops again to 4-6°C. A cross-plot between ΔSST and the Antarctic ice-core (EPICA Dome C (EDC)) temperature reconstruction supports the inference that ΔSST decreases as climate approaches peak cold and warm climate states and reaches highest values during intermediate climate conditions (Fig. 3a). This non-monotonic relationship between ΔSST and EDC temperature suggests that the latitudinal position of the PF has shifted as climate has changed.

To understand the impact of frontal shifts on the ΔSST between the selected core sites, we use a simple quantitative framework to simulate the response of individual site SST and ΔSST to different scenarios of coupling between PF latitude and regional climate (Fig. 3; also see Methods and Supplementary Figs. 5-14). In brief, we first simplified the modern surface layer temperature of the Kerguelen region taken from World Ocean Atlas 2018 into three segments. Then we applied different parameters to alter the three segments, mimicking different hypothetical PF changes. The parameters dictating this quantitative framework are the ranges of maximum temperature change in the AZ and the SAZ respectively, and the relationship between the changes in PF latitude and Antarctic climate (as represented by EDC temperature). In this study, we assume that the relationship between PF latitudinal change and Antarctic climate is linear. For the sensitivity tests, we investigated the evolution of ΔSST between the latitudes of MD11-3357 and MD11-3353 with different combinations of parameters. The results show that the non-monotonic relationship between ΔSST and EDC temperature only exists when the PF latitude shifts alongside Antarctic climate change (Supplementary Figs. 6 and 9), while the choice of different ranges of maximum temperature change in the AZ and the SAZ and different rates of PF migration with Antarctic climate change alters the shape of the non-monotonic pattern (see Supplementary Information).

To be consistent with polar amplification, we set the total range of glacial-interglacial temperature change in the AZ to be 2°C more than that in the SAZ and used optimization algorithm to define a relationship between PF latitude and Antarctic climate that best fits the TEX^{L}_{86}-reconstructed ΔSST between MD11-3357 and MD11-3353: Δlat (degrees) = ΔT_{EDC} (°C) * 0.66 + 4.33 (see Methods). Figure 3 compares the results of this optimized simulation with that of the simulation of no PF shift and the TEX^{L}_{86}-reconstructed SST data. In the simulation in which the location of the fronts is kept unchanged, the simulated ΔSST decreases when climate warms, which is consistent with polar amplification. This trend qualitatively matches that of the reconstructed ΔSST for the warmer climate intervals, but the simulated change in ΔSST is far too small (Fig. 3c *vs*. 3a). In addition, the simulation cannot reproduce the low ΔSST characteristic of the coldest conditions. In contrast, in the simulation in which PF latitude increases linearly with Antarctic temperature, the observed non-monotonic relationship between TEX^{L}_{86}-reconstructed ΔSST and EDC temperature is well-captured (Fig. 3e). Compared to the TEX^{L}_{86}-reconstructed ΔSST of the past 150,000 years, this simulation captures many temporal features (Fig. 3f). Thus, our simulation with latitudinal frontal shifts can account for the changes in the reconstructed ΔSST.

ACC frontal shifts over the last glacial cycle

Although modern observations suggest that the ACC may be locally restricted by bathymetry around the Kerguelen Plateau[56], the reconstructed ΔSST together with our quantitative framework suggest substantial shift of the frontal latitudes. At the beginning of the 21st century, about 2/3 of the ACC flow around the Kerguelen Plateau was deflected northwards, and the SAF was deflected southwards east of the Kerguelen Plateau[56]. Thus, overcoming topographic thresholds in the past might have caused major changes in the flow path of the ACC. To reconstruct past changes in PF latitudes, we use the best-fitting relationship between ΔSST and PF latitude changes inferred from our framework and the interpolated TEX^{L}_{86}-ΔSST between MD11-3353 and MD11-3357 to back-calculate the latitudinal changes of the position of the PF (Fig. 5d and Supplementary Fig. 16; see Methods). During cold intervals of the past, including MIS 2, MIS 4, and MIS 6, the low ΔSST implies a northward shift of the PF of up to ~2° compared to today (Fig. 5d). This northward shift is consistent with previous studies in the Indian sector of the Southern Ocean, but our estimated shift is smaller than the 5-10° northward shift that has been estimated based on sea-ice extent[35,57]. Ref. 33 estimated that the PF (defined as the θ_{min} 2°C, the 2°C subsurface isotherm at 200 m water depth) was located 2° north of site MD11-3353 during peak glacial conditions. The authors further suggested that an equatorward migration of the PF may be amplified by regional bathymetry and estimated a 6-7° northward shift of the PF in the Kerguelen region. Though potentially larger in other parts of the Southern Indian Ocean where the PF is subject to larger meandering, the glacial frontal shift reconstructed by our data and model for the Kerguelen region was ~2° northward of its current position.

According to our model, the temperature increase at MD11-3357 and MD11-3353 during the last two glacial terminations were associated with poleward shifts of the PF. This led to an initial increase followed by a decrease in the ΔSST (Fig. 2), as the steepest part of the SST profile first moved in between the two sites and then southward of both sites (Supplementary Fig. 5). The maximum ΔSST during Termination 2 remains lower than that of Termination 1 (Fig. 4). Due to the lower resolution of the SST data during Termination 2, it is likely that the brief period when the steepest part of the SST profile was sandwiched between the two sites was not well recorded, leading to a smaller maximum ΔSST. It is also possible that the exact slope of the SST profile may be different during the two terminations, producing a smaller increase in the ΔSST during the first half of Termination 2. However, the similar shape of the ΔSST progression when plotted over EDC temperature during the two terminations argues that they experienced similar changes in PF positions (Fig. 4). At the end of both terminations, ΔSST progressed to a lower range, signaling that the PF is most poleward at the beginning of interglacials.

During the previous interglacial (MIS 5e), SST at MD11-3357 and MD11-3353 were ~2-4°C warmer compared to pre-industrial, and the reconstructed ΔSST was very low (~4°C). This suggests that the PF remained at a southernly position after the end of Termination 2, such that the steepest part of the SST profile moved southward of the AZ core MD11-3353. Our reconstruction suggests a PF position of as much as 6.5° south during MIS 5e compared to today (Fig. 5d). These results agree well with previous estimates based on sea surface and subsurface temperature reconstructions from diatom and radiolarian assemblages[33]. Moreover, this is consistent with the unusually low biogenic opal fluxes at MD11-3353 during this interval, which may be related to silicate limitation on diatom growth as a consequence of a southward migration of the PF[58].

At the end of Termination 1/early Holocene, the PF reached as much as ~4.5° southward of the current position (Fig. 5d), in agreement with previous reconstructions[33]. This PF position would place the steepest part of the SST profile partly south of MD11-3353, explaining the low ΔSST of the early Holocene. During the late Holocene, while Antarctic temperatures remained stable, the reconstructed ΔSST increased from ~6°C to ~7.5°C (Fig. 2). This ΔSST increase is an upward line in the Antarctic (EDC) T-ΔSST space, deviating from the "horseshoe" trend of the last 150,000 years (Fig. 4). The increase in ΔSST since early Holocene suggests a gradual northward shift of the PF (Fig. 5d), which should correspond to a declining EDC temperature. Yet the EDC temperature remained stable during this interval. Here, we consider possible explanations for this deviation.

Because of interaction with local topography, the current PF to the west of the Kerguelen Plateau is shown to seasonally meander by as much as 4°[59]. As a result, unlike during MIS 5e when the PF was apparently locked in a position passing through the Fawn Trough south of the Kerguelen Plateau, the spatial relationship between the mean Holocene PF and the Kerguelen Plateau may have made the PF more prone to meander, producing greater scatter in the reconstructed ΔSST and possibly explaining the Holocene deviation from the "horseshoe". Ref. 33 suggested that the PF only briefly passed through Fawn Trough, which is ~5° southward of the current PF, and returned northward to its current position very early in the Holocene. Ref. 33 also observed a similar PF position for MIS 7, which is interpreted to be another more moderate interglacial, in contrast to the much southward position during the two warm interglacials MIS 5e and MIS 9. The southern Kerguelen bathymetry may help to explain the (lack of) poleward frontal shifts during moderate interglacials. As mentioned above, the bathymetric thresholds may be permanently surpassed in warmer interglacials such as MIS 5e, whereas during the Holocene this threshold was overcome only temporarily, and the PF shifted back northward quickly.

Another possibility is that Antarctic surface water temperature is decoupled from EDC temperature during the Holocene. The decrease in summer insolation at 65°N during the last 10,000 years is much smaller compared to that of 115,000-125,000 years ago, and its cooling effect through the albedo feedback is weak, mostly constrained to the extratropical Northern Hemisphere[60]. The decrease in obliquity during Holocene decreases the insolation received at high latitudes, but it may lead to relatively weak cooling effect at Antarctica inland ice core sites, as high albedo would result in little changes in net absorbed radiation, and stronger cooling at Antarctica continental margins and the surrounding Antarctic Ocean. As a result, temperature stayed stable at EDC for the last 10,000 years. At MD11-3353, the TEX^{L}_{86}-SST is shown to decline during the Holocene. SST reconstructions at different sites near the Western Antarctic Peninsula as well as the δD record at Taylor Dome also show a cooling trend for the last 10,000 years, tracking the decline in local insolation[61]. The cooling of the Antarctic Ocean would correspond with a northward shift of the PF, as predicted by our hypothesized quantitative framework, and supported by the ΔSST reconstruction and the results in ref. 33.

A related explanation, which will be discussed further below, involves the role of obliquity in Southern Ocean upwelling. Declining obliquity over the Holocene is expected to have strengthened the SWW thus northward Ekman surface water transport and upwelling in the AZ[62,63], consistent with N isotope reconstructions (Fig. 5f and g, ref. 20, 64). Independent of any change in the meridional position of the SWW, this would have pushed surface isotherms equatorward (i.e., increasing the meridional tilt of isopycnals)[65]. Thus, decoupling of PF position from Antarctic air temperature may be a fingerprint of obliquity-driven changes in upwelling.

Controls on ACC front latitudes

The temporal evolution of the PF position reconstructed from the ΔSST between MD11-3353 and MD11-3357 is generally correlated with changes in both ice core air temperature[44] and compiled Southern Ocean SST[66] (Fig. 5a, c and d), except for its decoupling from EDC temperature (but continued coupling with Southern Ocean SST) during the Holocene. Our findings are among the first quantitative evidence for the connection between Antarctic climate and the position of the PF. The low resolution of this first SST gradient-based PF latitude reconstruction limits comparison to other Southern Ocean records. However, several key correlations warrant noting.

The PF roughly delineates the northern limit of the wind-driven upwelling of Circumpolar Deep Water, and the latitude of the modern PF is correlated with the latitude of the SWW[54] (Fig. 1). Applying this causal relationship to frontal shifts in the Indian Southern Ocean during the last 150,000 years, the northward displacement of the PF during MIS 5d, 4, and 2 argue for coincident northward (equatorward) shifts of the SWW. Indeed, these intervals are associated with global cooling driven by changes in Earth's orbital parameters, which, according to global climate model simulations, should have driven an equatorward shift of the westerly winds as part of a cooling-driven contraction of the Hadley cell[62,67].

However, the cooling at MIS 5d does not bring global temperature to LGM conditions[68], while the coinciding equatorward shift of the PF does (Fig. 5c and d). The position of the SWW and thus upwelling in the Southern Ocean also responds to millennial-scale asymmetric climate changes between the northern and southern hemispheres. Modeling studies have shown that warming of the Southern Ocean during North Atlantic cold events would shift the SWW poleward[69], while terrestrial paleoclimate proxies suggest an equatorward shift of the SWW due to Southern Ocean cooling during the Antarctic Cold Reversal[70]. Unfortunately, the resolution of our records does not allow for investigation of the response of the PF to millennial-scale Heinrich events that led to asymmetric climate change of the two hemispheres, which may be the subject of future research using sediment cores of higher resolution.

As introduced previously, another important factor in the mid-latitude westerly winds is Earth's obliquity[63]. The reconstructed PF latitude over the last glacial cycle appears to partially covary with obliquity cycle, with a more northward PF associated with low obliquity (Fig. 5d and e). In global climate model simulations, lower obliquity can enhance the mid-latitude temperature gradient, which in turn drives intensification of the mid-latitude westerly winds[62,63,71,72]. In model simulations where changes in eddy flux only partially cancel out changes in wind-driven Ekman flow, an increase in wind strength would enhance the residual circulation of the Southern Ocean "upper cell" and increase transport of cold water northwards, leading to surface cooling to the north of the AZ[65], corresponding with a northward shift of the PF. The effect of obliquity on wind strength and upwelling intensity thus represents an additional mechanism that can explain the greater extent of equatorward frontal shift relative to that of global temperature drop at the end of MIS 5d, as well as the evident equatorward frontal shift during the late Holocene when the global cooling signal is weak.

Reciprocally, the location of the pronounced SST gradient is believed to impact the mid-latitude winds by anchoring the storm track around the oceanic front that maintains near-surface thermal gradients and energizes eddies in the lower troposphere, and a removal of the front results in substantial weakening of the eddy activity and the jet[73]. An initial meridional shift of the SST gradient field will induce positive feedbacks in the eddy activity that reinforce the shift, and this feedback is more pronounced for an equatorward-shifting SST front, although the equatorward shift is eventually inhibited by the presence of the subtropical jet[74]. This positive feedback process between the oceanic SST gradient and eddy-driven jet may help to explain the strength of northward frontal shift during MIS 5d.

Changes in upwelling and CO_2 outgassing

Changes in the latitude ranges of the ACC and the SWW may have important consequences for the release of respired carbon from the deep ocean through its communication with the atmosphere in the Southern Ocean. A northward shift in the SWW would weaken the ACC flow that can pass through the Drake Passage and decrease upwelling of deep water in the "upper cell" of the overturning circulation in Antarctica[21], which would promote deep carbon storage through a combination of mechanisms[17]. In addition, decreased upwelling of the relatively warmer Circumpolar Deep Water under more equatorward SWW would promote the expansion of quasi-permanent sea ice and shoal the density interface between the lower and upper cell of the Southern Ocean overturning[11], decreasing the deep turbulent mixing and isolate Antarctic Bottom Water from the other water masses in the ocean interior, keeping more CO_2 in the deep ocean[75,76].

While we have just argued for a strong correlation between atmospheric CO_2 concentration and the latitudinal position of the PF, comparing the atmospheric CO_2 record[77] with our reconstructed PF latitude shows several discrepancies. Specifically, the PF shifted strongly northward at MIS 5d while CO_2 declined only modestly, and the PF shifted northward through the Holocene while the CO_2 rose (Fig. 5a and d). These discrepancies may be explained by changes in the intensity of AZ upwelling (as reconstructed with diatom-bound $\delta^{15}N$, Fig. 5g; ref. 20) that do not have a direct connection to the mean latitude of the westerly winds. The low obliquity at MIS 5d and the declining obliquity during the Holocene should have increased the temperature gradient between the middle and high latitudes, which is supported by the increase in temperature difference between moisture source and ice core site of Vostok[78]. This increase in temperature gradient should have intensified the SWW, compensating for the equatorward displacement of the winds so as to maintain and/or increase upwelling and thus permit CO2 outgassing from the AZ[20]. In addition, as described above, the strong SWW-driven (Ekman) transport of AZ surface waters northward driven by low(ering) obliquity at MIS 5d and the Holocene may have worked to push surface isotherms northward. Together, these processes can explain the otherwise anomalous conditions of MIS 5d and the late Holocene of a northward PF (Fig. 5d), strong AZ upwelling (Fig. 5g), and relatively high atmospheric CO_2 (Fig. 5a and b). The compiled data (Fig. 5) suggest that the role of obliquity on AZ upwelling was muted during the coldest climates of the last glacial cycle, becoming important only during moderate and warm climates. This observation may be the result of a stronger subtropical jet under warm global mean climate[79], which leads to a greater amplitude of change associated with its modulation by obliquity.

Conclusions

Applying the TEX^{L}_{86} paleotemperature proxy to two sediment cores in the Indian sector of the Southern Ocean, we reconstruct their SST difference (ΔSST) over the last glacial cycle. Using a simple quantitative framework for the relationship between ΔSST and the position of the Antarctic Polar Front (PF), we show that the reconstructed ΔSST cannot be a consequence of polar amplification alone but rather points to coherent PF displacements that are linearly correlated with Antarctic temperature. We report lower ΔSST in combination with lower Antarctic temperatures, during MIS 2, 4 and 6, suggesting a northward shift of the PF of up to 2° latitude. Conversely, lower ΔSST and higher Antarctic temperatures are consistent with a southward shift of the PF of up to 6° latitude during MIS5e (Fig. 5d). While our results are consistent with previous proposals[17,21], some data-based studies[31–35,38], and some model predictions[62,67], the approach taken here provides a more quantitative, temporally continuous view of PF history purely based on SST. With generation of additional SST records in the Southern Ocean and refinements in age models, this approach promises to provide multiple constraints on the climatic controls on PF location and Southern Ocean circulation.

We suggest that global cooling was a dominant driver of the equatorward shift of the SWW during the ice ages, with changes in the wind strength driven by obliquity also contributing to reconstructed changes. Through its effects on Southern Ocean upwelling and related vertical circulation, the equatorward shift of the SWW during ice ages should have enhanced the storage of carbon in the deep ocean, helping to explain the lower atmospheric CO_2 levels of the ice ages. During MIS 5d and the late Holocene, low obliquity and thus an increased mid-latitude temperature gradient may have strengthened the westerly wind-driven AZ upwelling, compensating for the equatorward jet location so as to sustain the upwelling in the AZ and thus raising atmospheric CO_2 somewhat while also pushing the PF northward during these special time intervals. Thus, the effects of obliquity change may explain the deviation of MIS 5d and the late Holocene from the overarching tendency over the glacial cycle for a more northward PF to be associated with global cooling, reduced AZ upwelling, and lower atmospheric CO_2.

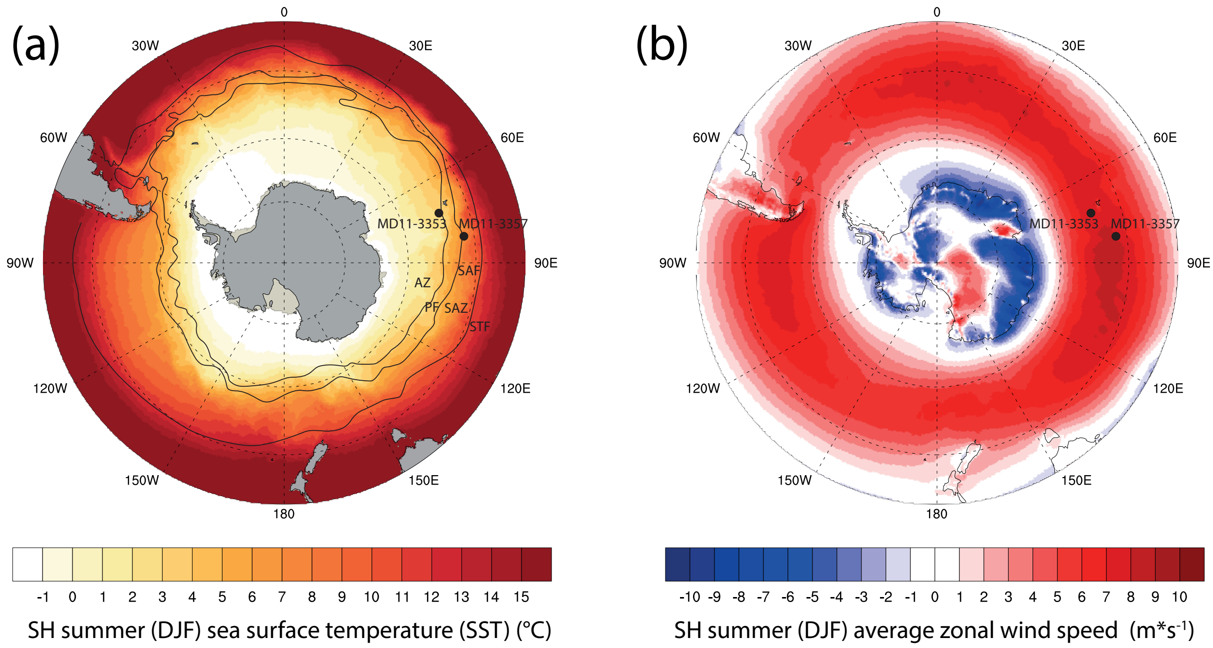

Figure 1: Maps of modern Southern Ocean sea surface temperature (SST) and 10 m zonal wind strength in austral summer. Austral summer (DJF) (a) SST (°C) and (b) 10 m zonal wind strength ($m \cdot s^{-1}$) based on reanalysis data for the period 1951-1990[80,81]. Black circles indicate core locations MD11-3353 (50.57°S, 68.39°E) in the AZ and MD11-3357 (44.68°S, 80.43°E) in the SAZ. STF = Subtropical Front, SAF = Subantarctic Front, PF = Polar Front, SAZ = Subantarctic Zone, AZ = Antarctic Zone, after ref. 25.

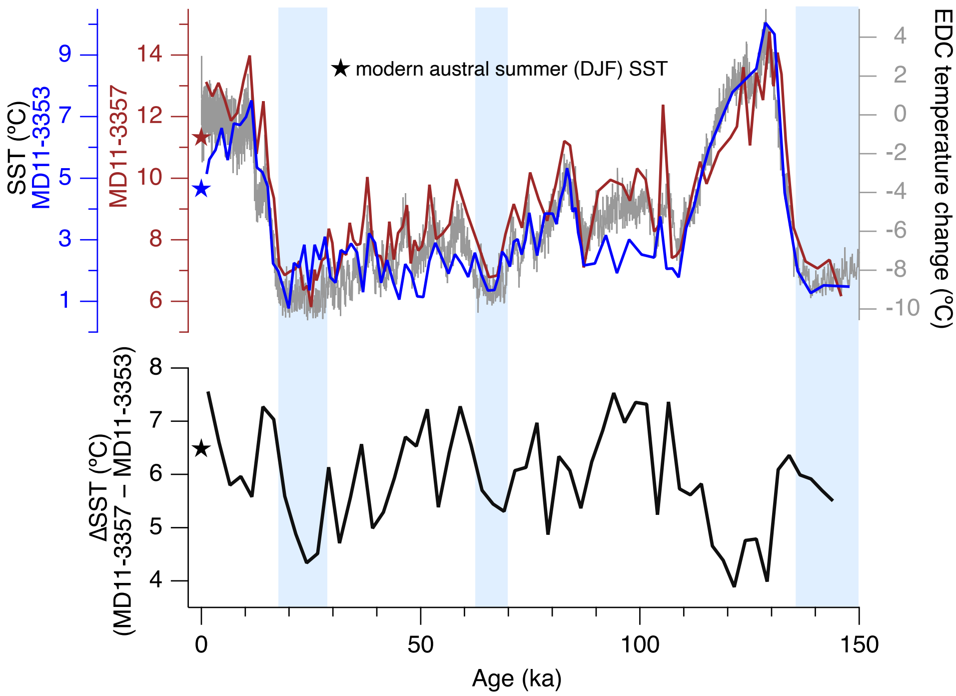

Figure 2: SST reconstructions through the last glacial cycle. Top: GDGT-based (TEX^{L}_{86}) SST reconstruction for SAZ core MD11-3357 (red) and AZ core MD11-3353 (blue), compared to the EDC δD record[44] (grey). Bottom: SST difference (ΔSST) between the two cores, SST(MD11-3357) – SST(MD11-3353), calculated on a 2,500-year-resolution x-axis. Vertical bars in blue indicate cold periods MIS 2, 4, and 6. Stars indicate modern austral summer (DJF) SST[43].

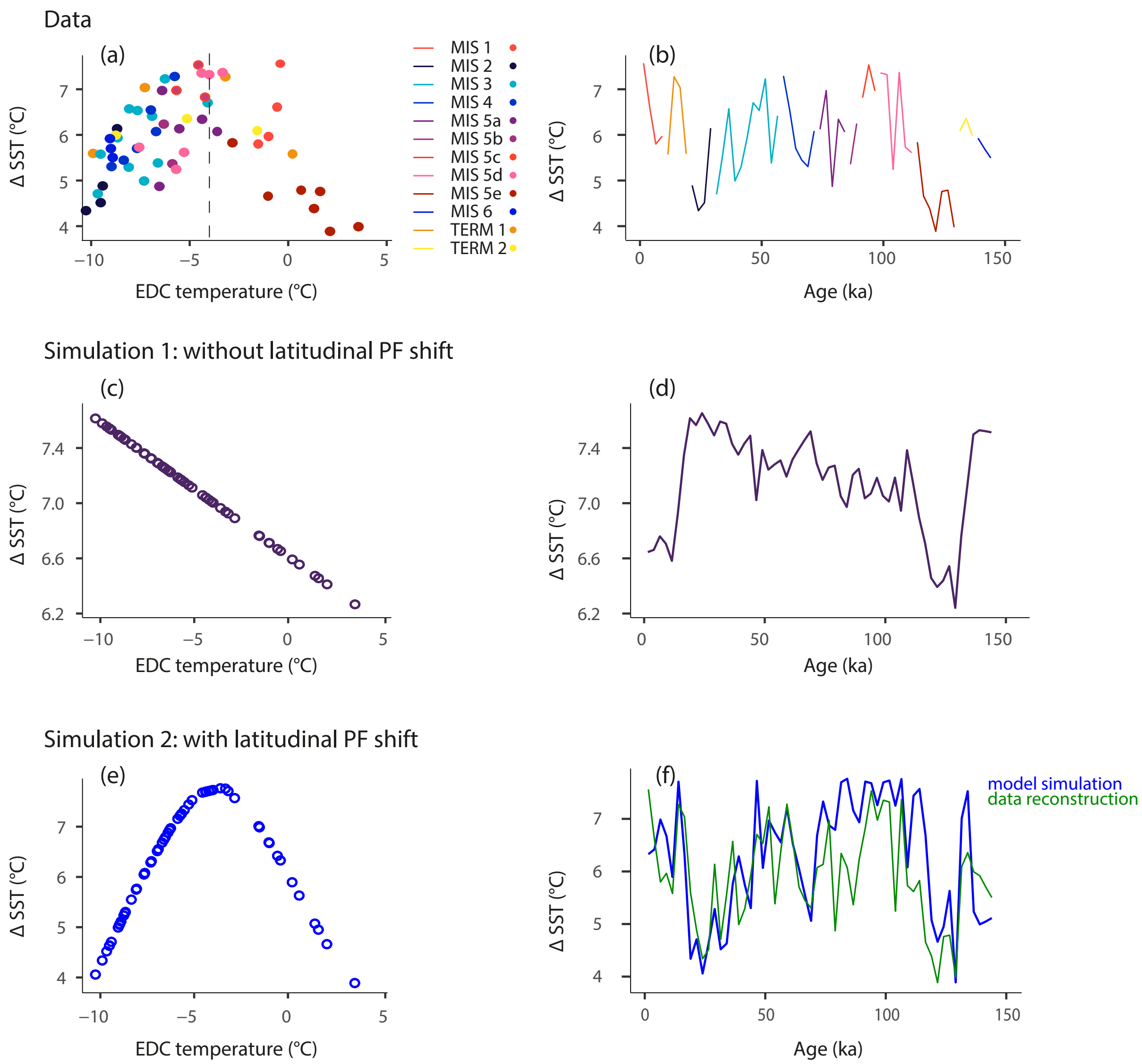

Figure 3: Date-simulation comparison of the relationship between Antarctic air temperature and the sea surface temperature difference (ΔSST) between the two Southern Ocean sediment cores. (a) The reconstructed ΔSST plotted against the EDC temperature depicts a horseshoe pattern with its angular point (largest ΔSST) around −4°C (dotted line). The color code (red colors represent warm intervals and blue colors cold intervals) shows that MIS 5e has the smallest ΔSST together with warmest EDC temperatures. (b) The downcore record of reconstructed ΔSST between MD11-3357 and MD11-3353. (c and d) Simulated ΔSST between the latitude of MD11-3357 and that of MD11-3353 without PF shift plotted over EDC temperature and age. (e) Simulated ΔSST with the optimized parameters of PF shift plotted over EDC temperature age. (f) Comparison of simulated ΔSST and reconstructed ΔSST of the last 150,000 years.

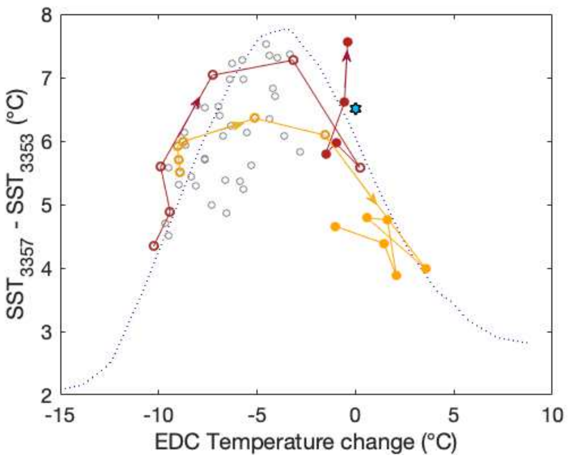

Figure 4: Data for Termination 1 and Termination 2. Reconstructed ΔSST (circles) and simulated ΔSST (dotted line) plotted over EDC temperature change[44]. Red open circles represent data of Termination 1 (10,000-19,000 years ago), and red filled circles represent data of Holocene (0-10,000 years ago). The red line and arrow represent the temporal progression of ΔSST towards younger ages. Orange open circles represent data of Termination 2 (129,000-144,000 years ago), and orange filled circles represent data of MIS 5e (115,000-129,000 years ago). The orange line and arrow represent the temporal progression of the ΔSST towards younger ages. The blue asteroid represents the modern WOA data[43].

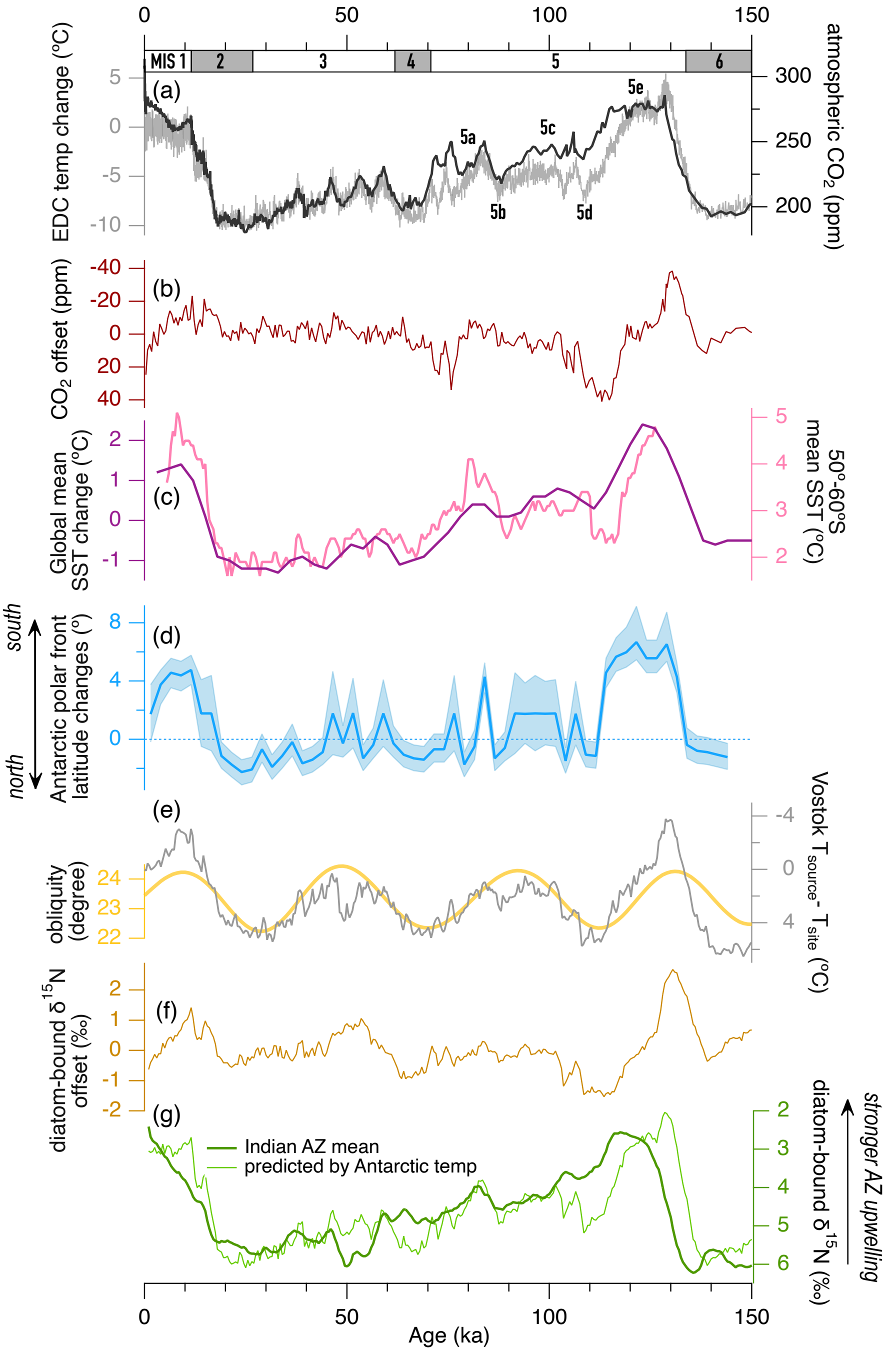

Figure 5: ACC-associated frontal shifts over the last glacial cycle and their connections to climate and CO_2 change. (a) atmospheric CO_2 reconstructions[77] (black) and EDC temperature record[44] (grey), (b) Offset between CO_2 and predicted CO_2 based on a linear relationship between Antarctic ice core temperature and CO_2 [20] (dark red), (c) Compilation of SST at 50°-60°S[66] (pink) and global SST change[68] (purple), (d) Changes in PF latitude calculated from ΔSST (3357–3353) (thick sky blue line) and the uncertainty bounds (lighter shading), (e) changes in the difference between the air temperature at the moisture source (T_{source}) and ice core site (T_{site}) of Vostok[78] (dark grey) relative to modern conditions,

reconstructed from ice deuterium excess, and obliquity[82] (yellow), (f) Offset between Indian AZ diatom-bound $\delta^{15}N$ and predicted diatom-bound $\delta^{15}N$ based on a linear relationship between Antarctic air temperature and diatom-bound $\delta^{15}N$[20] (brown), (g) Combined record of Indian AZ diatom-bound $\delta^{15}N$ as an indicator of upwelling[20] (dark green) and predicted diatom-bound $\delta^{15}N$ based on a linear relationship between Antarctic air temperature and diatom-bound $\delta^{15}N$[20].

Methods

Study area

Marine sediment cores MD11–3353 (50.57°S, 68.39°E, 1.568 m water depth) and MD11–3357 (44.68°S, 80.43°E, 3.349 m water depth) were recovered by the *R.V. Marion Dufresne* in 2011 and 2012 around the Kerguelen Archipelago in the southwest Indian Ocean (Fig. 1). Both cores were recently described elsewhere[20,58,64]. MD11-3353 is located slightly south of the modern Antarctic Polar Front (PF), whereas MD11-3357 is located in the Subantarctic Zone (SAZ), just north of the Subantarctic Front (SAF). The close proximity of the Subtropical Front (STF) in the north defines a narrow SAZ domain in this region[56]. The Kerguelen Plateau exerts a strong influence on the ACC flow such that a 60% of the current is deflected northwards of the Plateau, followed by a southeastward flow east of the plateau and the integrated ACC flow is estimated to reach 150 Sv around the Kerguelen Plateau[56].

Age models

This study relies on previously published age models for all cores[20,58]. Briefly, the age model for MD11–3357 relies on graphical alignment of the GDGT-based SST reconstruction with the EDC deuterium record[44,58]. The original age model for MD11-3353[58], aligning GSGT-based SST with the EDC deuterium record[44], has been updated by adjusting the youngest and oldest tie points and adding two tie points in MIS 3 based on diatom-bound $\delta^{15}N$ correlation with the diatom-bound $\delta^{15}N$ record of MD12-3394[20].

SST reconstructions

SST reconstructions are based on measurements of glycerol dialkyl glycerol tetraethers (GDGTs) which are produced by pelagic *Thaumarchaeota*[83]. The sea surface temperature index TEX_{86} is based on the temperature sensitivity of the average numbers of cyclopentane moieties found in these archaeal lipids[40]. GDGT measurements followed the method proposed in ref. 84. Briefly, the GDGT-fraction was extracted from 3–5 g of freeze-dried sediment and simultaneously separated from other organic biomarkers using an Accelerated Solvent Extractor (ASE 350) and analyzed with a high-pressure liquid chromatograph coupled to a single quadrupole mass spectrometer detector (HPLC-MS; Agilent 1260 Infinity)[85]. Intralaboratory standard SST error for replicate measurements of a standard sediment sample extracted in each batch of samples (n=13) was 0.5°C, i.e. similar to literature estimates[86]. SST was reconstructed using the TEX^{L}_{86} calibration in ref. 42 to reconstruct changes in SST, which produces better glacial-interglacial pattern in the high latitude regions[20,41,87] (Supplementary Fig. 1 and 2). We estimated the potential contribution of isoprenoid GDGTs from non-*Thaumarchaeota* sources on the estimated TEX^{L}_{86} temperatures using a series of GDGT-based indices (Supplementary Fig. 3). All the samples analyzed were within the expected values for pelagic *Thaumarchaeota* GDGT producers, indicating negligible contributions from other sources.

ΔSST calculation

To calculate past ΔSST, the data from different cores have been resampled following a linear interpolation with a resampling step of 2,500 years, which best resembles the initial resolution in both cores.

ΔSST was then determined by subtraction:

$$\Delta SST_{(core\ 1-core\ 2)tx} = SST_{core\ 1,tx} - SST_{core\ 2,tx} \qquad (eq. 1)$$

with t_x describing the same age point in the cores, core 1 being MD11-3357 and core 2 being MD11-3353.

Quantitative framework setup

The initial SST profile is the zonally averaged mean summer temperatures of 0-200m depth of the region 68.5°E to 80.5°E, 34.5°S to 60.5°S from World Ocean Atlas 2018[43], which is the representative growth season and depth of the GDGT-producing archaea blooms[42,87]. The initial SST profile is simplified to three segments: the AZ segment, the PFZ segment, and the SAZ segment (Supplementary Fig. 5). From higher to lower latitudes, the AZ-PFZ boundary (denoted $lat1$) and PFZ-SAZ boundary (denoted $lat2$) are the latitudes with the largest increase and decrease in the slope of the SST profile, respectively. These changes in slope represent the transition from the relatively well-mixed cold polar surface water mass towards the warm surface waters of the SAZ. The SST within each segment were then fitted to a linear line:

$$SST_{AZ}(lat) = k_{AZ} * lat + m_{AZ}, lat < lat1$$

$$SST_{PFZ}(lat) = k_{PFZ} * lat + m_{PFZ}, lat1 < lat < lat2$$

$$SST_{SAZ}(lat) = k_{SAZ} * lat + m_{SAZ}, lat > lat1$$

EDC relative air temperatures were used as a reflection of Antarctic climate change. Temperature changes at EDC were transferred into different amounts of temperature change in the AZ and the SAZ due to polar amplification. Two parameters, $range_{AZ}$ and $range_{SAZ}$, represent the maximum temperature change (i.e., peak interglacial SST minus peak glacial SST) in the two regions. For any given EDC temperature change at time t, we assume that the SST of the AZ and SAZ will increase/decrease a fraction of the maximum temperature range of the zone, and we can get the SST lines in the AZ and the SAZ at time t (Supplementary Fig. 5, with the constraint that the lowest SST is −2°C for the AZ, the freezing point of sea water):

$$SST_{AZ}(t, lat)_{no\ shift} = k_{AZ} * lat + m_{AZ} + \frac{\Delta T_{EDC}(t)}{max(\Delta T_{EDC}) - \min(\Delta T_{EDC})} * range_{AZ}, lat < lat1$$

$$SST_{SAZ}(t, lat)_{no\ shift} = k_{SAZ} * lat + m_{SAZ} + \frac{\Delta T_{EDC}(t)}{max(\Delta T_{EDC}) - \min(\Delta T_{EDC})} * range_{SAZ}, lat > lat2$$

The new SST line of the PFZ segment at time t is a linear line between the new temperatures at $lat1$ and $lat2$. (Supplementary Fig. 5):

$$SST_{PFZ}(t, lat)_{no\ shift} = \frac{SST_{SAZ}(t, lat2)_{no\ shift} - SST_{AZ}(t, lat1)_{no\ shift}}{lat2 - lat1} * lat + m'_{PFZ},$$

$$lat1 < lat < lat2$$

We then assume that a change in Antarctic temperature leads to a latitudinal shift of all three SST lines, and the amount of shift is linearly related to the amount of EDC temperature change:

$$\Delta lat(t) = a * \Delta T_{EDC}(t) + b \ (\Delta lat > 0\ represents\ a\ poleward\ shift)$$

The SST lines after the shift are:

$$SST_{AZ}(t, lat)_{shift} = k_{AZ} * \left(lat + \Delta lat(t)\right) + m_{AZ} + \frac{\Delta T_{EDC}(t)}{max(\Delta T_{EDC}) - \min(\Delta T_{EDC})} * range_{AZ},$$

$$lat + \Delta lat(t) < lat1$$

$$SST_{SAZ}(t, lat)_{shift} = k_{SAZ} * \left(lat + \Delta lat(t)\right) + m_{SAZ} + \frac{\Delta T_{EDC}(t)}{max(\Delta T_{EDC}) - \min(\Delta T_{EDC})} * range_{SAZ},$$

$$lat + \Delta lat(t) > lat2$$

$$SST_{PFZ}(t, lat)_{shift} = \frac{SST_{SAZ}(t, lat2)_{no\ shift} - SST_{AZ}(t, lat1)_{no\ shift}}{lat2 - lat1} * (lat + \Delta lat(t)) + m'_{PFZ},$$

$$lat1 < (lat + \Delta lat(t)) < lat2$$

Determination of the optimal parameters

To tune our model to match the reconstructed ΔSST, we need to determine the four unknown parameters: the maximum range of temperature change in the AZ and SAZ, i.e. $range_{AZ}$ and $range_{SAZ}$, and the slope and intercept of the linear relationship between Δlat and ΔT_{EDC}, i.e. a and b. The sensitivity analysis shows that $range_{AZ}$ and $range_{SAZ}$ have little impact on when the maximum ΔSST occurs, thus we tentatively chose 3°C to be $range_{AZ}$ and 1°C to be $range_{SAZ}$, based on different reconstructions glacial temperature reconstructions[51,66].

The sensitivity analysis also shows that with realistic values for a, the maximum ΔSST between the two sites would occur when the PF is ~1.8° southward of its current position (Supplementary Fig. 7 and 10). The maximum TEX^L_{86}-reconstructed ΔSST occurs when the temperature change at EDC is around −3°C to −5°C (Supplementary Fig. 12). We took the group of the data with EDC temperature between −3°C and −5°C and calculated their mean EDC temperature change and the mean ΔSST, which are ~-4°C and 7°C respectively (Supplementary Fig. 12). This suggests that during the past 150,000 years, the PF was around 1.8° southward when the EDC temperature was around −4°C lower than the present:

$$\Delta lat(\max SST grad) = a * \Delta T_{EDC}(\max SST grad) + b = a * (-4) + b = 1.8$$

Based on the sensitivity tests, we took −2° (2° northward) to be the estimated PF position for the mean peak glacial, which is defined as EDC temperatures lower than −9°C and has a mean EDC temperature change of −9.6°C and mean ΔSST of 5.1°C (Supplementary Fig. 12):

$$\Delta lat(\text{peak glacial}) = a * \Delta T_{EDC}(peak\ glacial) + b = a * (-9.6) + b = -2$$

With these two equations, we calculated that $a = 0.68$, $b = 4.52$. The physical meaning of a is that for every degree Celsius of EDC temperature warming(cooling), there is a 0.68° southward(northward) latitudinal shift in the position of the PF. The physical meaning of b is that when EDC is at its current temperature ($\Delta T_{EDC} = 0$), the position of the PF is 4.52° southward of the initial position. However, the initial scenario is the modern SST profile, which should have a Δlat of 0. The inconsistency of the modern SST profile and the PF position predicted by the model with the EDC ice core-top temperature leads us to consider the possibility that the modern PF position is an "outlier" comparing to the frontal movement from MIS 6 to MIS 2 and we should consider a new initial SST profile.

A straight-forward option is to choose the scenario when the steep PFZ segment is optimally sandwiched in between the core's locations as the new initial profile. This would also be the scenario when ΔSST is the largest. According to the TEX^L_{86}-reconstructed data, this scenario would be when the temperature change at EDC is around −4°C and the PF is around 1.8° southward of its current position. However, the exact SST profile of this time is unknown. According to the TEX^L_{86}-reconstructed data, when the EDC temperature change was between −3°C and −5°C, the frontal shift placed the steep PFZ segment between MD11-3353 and MD11-3357, and the mean value of the ΔSST is ~7°C, which is similar to the temperature difference between the two endpoints of the PFZ segment in the current WOA SST profile, which is ~7.6°C. Thus, it is a fair estimate that the new initial scenario is the current WOA profile shifted 1.8° southward, at the time when the EDC temperature change was −4°C. The actual SST profile may be higher or lower than our assumed profile, but for the ΔSST, the difference in the absolute value will be canceled off. We defined $\Delta lat'$ as the PF latitude relative to the new initial profile, and the relationship between Δlat and ΔT_{EDC} becomes:

$$\Delta lat' = \Delta lat - 1.8 = a' * \ \Delta T'_{EDC} + b' = \ a' * [\Delta T_{EDC} - (-4)] + b'$$

As previously, we took $range_{AZ}$ = 3°C, and $range_{SAZ} = 1$ °C and used sequential least squares programming (SLSQP) optimizer in Python to find a' within [0, +inf] and b' within [-inf, +inf] that best fit the reconstructed data. The resulting a' and b' with realistic values that produce the smallest difference between the modeled results and the actual data is 0.66 and −0.11 respectively (Supplementary Fig. 14):

$$\Delta lat - 1.8 = 0.66 * \Delta T'_{EDC} - 0.11 = \ 0.66 * [\Delta T_{EDC} - (-4)] - 0.11$$

$$\Delta lat = 0.66 * \ \Delta T_{EDC} + 4.33$$

With this best-fitting pair of a' and b', the PF shifts southward(northward) by ~0.66° with every °C of EDC warming(cooling). When EDC temperature change is 0 relative to the modern ($\Delta T_{EDC} = 0$), the PF is 4.33° south of its current position ($\Delta lat = 4.33$). This pair of parameters is very similar to the parameters we calculated using the WOA as the initial SST profile, which shows that these optimal parameters are robust.

When applying these parameters to the model with the three-segment simplified SST lines, the maximum ΔSST is around 8.6°C. This high value derives from the over-estimation of the SST difference between the two boundary latitudes $lat1$ and $lat2$ in the simplified three-segment SST line. To correct this, for each change in EDC temperature — after the associated shifts in the intercept of the AZ and SAZ segment lines — we smooth the SST lines back into curves by calculating the offset between the original WOA profile and the original three-segment lines and adding this offset back to the new three-segment lines. Shifting the smoothed curves latitudinally gives a flatter “horse-shoe” shape that better matches the reconstructed data (Supplementary Fig. 13).

Reconstruction of PF latitude changes in the past 150,000 years

Based on the modelled relationship between the ΔSST of sites MD11-3357 and MD11-3353 and the change of PF latitude, we use the reconstructed TEX^{L}_{86}-SST at the two sites to reconstruct the relative PF positions of the 150,000 years. Because the relationship is non-monotonic, within the relevant range, each ΔSST corresponds to two PF positions, and we select the position that makes more sense for the corresponding EDC temperature in our optimized model: If the EDC temperature is lower than −4°C, we choose the latitude that is more southward than 1.8° (the upper part of the curve in Supplementary Fig. 16). The standard deviation of TEX^{L}_{86}-reconstructed ΔSST is conservatively set to be 1°C. When ΔSST is higher than 6.7°C, the two estimated PF positions are close that their confidence intervals merge. In this case we take the average of the two PF positions to be the estimated position, and the combined confidence interval to be the uncertainty range for this estimate.

Acknowledgments

We gratefully thank H. Eri Amsler, Julia Gottschalk, Thomas Frölicher, Gianna Battaglia, Fortunat Joos and Xavier Crosta for fruitful discussions. We thank Bichen Zhang for help with setting up the quantitative framework.

Financial support for this study was provided by the Swiss National Science Foundation (grants P1BEP2_168625 to LMT and PP00P2_144811 and PP00P2_172915 to SLJ), the Max Planck Society (AMG), and the ERC starting GRANT OceaNice (PKB).

Author Contributions

LMT, XEA, SLJ, AMG and DMS devised the study. LMT, AA, SM and MS performed the GDGT analyses supervised by AMG. LMT calculated the SST difference between the two sites. XEA set up the quantitative framework and ran simulations. MW performed the modern data re-analyses. EM and AM planned the cruise to retrieve the sediment cores presented here. LMT and XEA wrote the manuscript with contributions from all co-authors.

Competing interests

The authors declare no competing interests.

Data availability

The SST datasets used in this study are available from the PANGAEA database.

Code availability

MATLAB and Python code used for data analysis and quantitative framework simulations are available from the corresponding author upon request.

References

1. Sabine, C. L. *et al.* The Oceanic Sink for Anthropogenic CO_2. *Science* (2004) doi:10.1126/science.1097403.
2. Khatiwala, S., Primeau, F. & Hall, T. Reconstruction of the history of anthropogenic CO_2 concentrations in the ocean. *Nature* **462**, 346–349 (2009).
3. Shi, J.-R., Xie, S.-P. & Talley, L. D. Evolving Relative Importance of the Southern Ocean and North Atlantic in Anthropogenic Ocean Heat Uptake. *Journal of Climate* **31**, 7459–7479 (2018).
4. Armour, K. C., Marshall, J., Scott, J. R., Donohoe, A. & Newsom, E. R. Southern Ocean warming delayed by circumpolar upwelling and equatorward transport. *Nature Geosci* **9**, 549–554 (2016).
5. Quéré, C. L. *et al.* Saturation of the Southern Ocean CO_2 Sink Due to Recent Climate Change. *Science* (2007) doi:10.1126/science.1136188.
6. Landschützer, P. *et al.* The reinvigoration of the Southern Ocean carbon sink. *Science* (2015) doi:10.1126/science.aab2620.
7. DeVries, T., Holzer, M. & Primeau, F. Recent increase in oceanic carbon uptake driven by weaker upper-ocean overturning. *Nature* **542**, 215–218 (2017).
8. Burke, A. & Robinson, L. F. The Southern Ocean's Role in Carbon Exchange During the Last Deglaciation. *Science* (2012) doi:10.1126/science.1208163.
9. Skinner, L. C., Fallon, S., Waelbroeck, C., Michel, E. & Barker, S. Ventilation of the Deep Southern Ocean and Deglacial CO_2 Rise. *Science* (2010) doi:10.1126/science.1183627.
10. Keeling, R. F. & Stephens, B. B. Antarctic sea ice and the control of Pleistocene climate instability. *Paleoceanography* **16**, 112–131 (2001).

11. Ferrari, R. *et al.* Antarctic sea ice control on ocean circulation in present and glacial climates. *PNAS* **111**, 8753–8758 (2014).

12. Martin, J. H. Glacial-interglacial CO2 change: The Iron Hypothesis. *Paleoceanography* **5**, 1–13 (1990).

13. Martínez-García, A. *et al.* Iron Fertilization of the Subantarctic Ocean During the Last Ice Age. *Science* **343**, 1347–1350 (2014).

14. François, R. *et al.* Contribution of Southern Ocean surface-water stratification to low atmospheric CO2 concentrations during the last glacial period. *Nature* **389**, 929–935 (1997).

15. Watson, A. J. & Naveira Garabato, A. C. The role of Southern Ocean mixing and upwelling in glacial-interglacial atmospheric CO2 change. *Tellus B: Chemical and Physical Meteorology* **58**, 73–87 (2006).

16. Watson, A. J., Vallis, G. K. & Nikurashin, M. Southern Ocean buoyancy forcing of ocean ventilation and glacial atmospheric CO2. *Nature Geosci* **8**, 861–864 (2015).

17. Sigman, D. M. *et al.* The Southern Ocean during the ice ages: A review of the Antarctic surface isolation hypothesis, with comparison to the North Pacific. *Quaternary Science Reviews* **254**, 106732 (2021).

18. Studer, A. S. *et al.* Antarctic Zone nutrient conditions during the last two glacial cycles. *Paleoceanography* **30**, 845–862 (2015).

19. Wang, X. T. *et al.* Deep-sea coral evidence for lower Southern Ocean surface nitrate concentrations during the last ice age. *Proc Natl Acad Sci USA* **114**, 3352–3357 (2017).

20. Ai, X. E. *et al.* Southern Ocean upwelling, Earth's obliquity, and glacial-interglacial atmospheric CO_2 change. *Science* **370**, 1348–1352 (2020).

21. Toggweiler, J. R., Russell, J. L. & Carson, S. R. Midlatitude westerlies, atmospheric CO_2, and climate change during the ice ages: westerlies and CO_2 during the ice ages. *Paleoceanography* **21**, n/a-n/a (2006).

22. Anderson, R. F. *et al.* Wind-Driven Upwelling in the Southern Ocean and the Deglacial Rise in Atmospheric CO_2. *Science* **323**, 1443–1448 (2009).

23. Toggweiler, J. R. & Russell, J. Ocean circulation in a warming climate. *Nature* **451**, 286–288 (2008).

24. Marshall, J. & Speer, K. Closure of the meridional overturning circulation through Southern Ocean upwelling. *Nature Geosci* **5**, 171–180 (2012).

25. Orsi, A. H., Whitworth, T. & Nowlin, W. D. On the meridional extent and fronts of the Antarctic Circumpolar Current. *Deep Sea Research Part I: Oceanographic Research Papers* **42**, 641–673 (1995).

26. Sokolov, S. & Rintoul, S. R. Circumpolar structure and distribution of the Antarctic Circumpolar Current fronts: 1. Mean circumpolar paths. *Journal of Geophysical Research: Oceans* **114**, (2009).

27. Graham, R. M., de Boer, A. M., Heywood, K. J., Chapman, M. R. & Stevens, D. P. Southern Ocean fronts: Controlled by wind or topography? *Journal of Geophysical Research: Oceans* **117**, (2012).

28. Böning, C. W., Dispert, A., Visbeck, M., Rintoul, S. R. & Schwarzkopf, F. U. The response of the Antarctic Circumpolar Current to recent climate change. *Nature Geosci* **1**, 864–869 (2008).

29. Saenko, O. A., Fyfe, J. C. & England, M. H. On the response of the oceanic wind-driven circulation to atmospheric CO2 increase. *Climate Dynamics* **25**, 415–426 (2005).

30. Munday, D. R., Johnson, H. L. & Marshall, D. P. Eddy Saturation of Equilibrated Circumpolar Currents. *Journal of Physical Oceanography* **43**, 507–532 (2013).

31. Bostock, H. C. *et al.* A review of the Australian–New Zealand sector of the Southern Ocean over the last 30 ka (Aus-INTIMATE project). *Quaternary Science Reviews* **74**, 35–57 (2013).
32. Nair, A. *et al.* Southern Ocean sea ice and frontal changes during the Late Quaternary and their linkages to Asian summer monsoon. *Quaternary Science Reviews* **213**, 93–104 (2019).
33. Civel-Mazens, M. *et al.* Antarctic Polar Front migrations in the Kerguelen Plateau region, Southern Ocean, over the past 360 kyrs. *Global and Planetary Change* **202**, 103526 (2021).
34. Manoj, M. C. & Thamban, M. Shifting frontal regimes and its influence on bioproductivity variations during the Late Quaternary in the Indian sector of Southern Ocean. *Deep Sea Research Part II: Topical Studies in Oceanography* **118**, 261–274 (2015).
35. Gersonde, R., Crosta, X., Abelmann, A. & Armand, L. Sea-surface temperature and sea ice distribution of the Southern Ocean at the EPILOG Last Glacial Maximum—a circum-Antarctic view based on siliceous microfossil records. *Quaternary Science Reviews* **24**, 869–896 (2005).
36. Brathauer, U. & Abelmann, A. Late Quaternary variations in sea surface temperatures and their relationship to orbital forcing recorded in the Southern Ocean (Atlantic sector). *Paleoceanography* **14**, 135–148 (1999).
37. Kohfeld, K. E. *et al.* Southern Hemisphere westerly wind changes during the Last Glacial Maximum: paleo-data synthesis. *Quaternary Science Reviews* **68**, 76–95 (2013).
38. Gray, W. *et al.* Poleward shift in the Southern Hemisphere westerly winds synchronous with the deglacial rise in CO2. Preprint on *Research Square* (2022). doi:10.21203/rs.3.rs-404786/v1.

39. Sigman, D. M. & Boyle, E. A. Glacial/interglacial variations in atmospheric carbon dioxide. *Nature* **407**, 859–869 (2000).

40. Schouten, S., Hopmans, E. C., Schefuß, E. & Sinninghe Damsté, J. S. Distributional variations in marine crenarchaeotal membrane lipids: a new tool for reconstructing ancient sea water temperatures? *Earth and Planetary Science Letters* **204**, 265–274 (2002).

41. Kim, J.-H. *et al.* New indices and calibrations derived from the distribution of crenarchaeal isoprenoid tetraether lipids: Implications for past sea surface temperature reconstructions. *Geochimica et Cosmochimica Acta* **74**, 4639–4654 (2010).

42. Kim, J.-H. *et al.* Holocene subsurface temperature variability in the eastern Antarctic continental margin. *Geophysical Research Letters* **39**, (2012).

43. Locarnini, M. *et al.* World Ocean Atlas 2018, Volume 1: Temperature. (2018).

44. Jouzel, J. *et al.* Orbital and Millennial Antarctic Climate Variability over the Past 800,000 Years. *Science* **317**, 793–796 (2007).

45. Martínez-Garcia, A. *et al.* Links between iron supply, marine productivity, sea surface temperature, and CO2 over the last 1.1 Ma. *Paleoceanography* **24**, (2009).

46. Sikes, E. L. *et al.* Southern Ocean seasonal temperature and Subtropical Front movement on the South Tasman Rise in the late Quaternary. *Paleoceanography* **24**, (2009).

47. Ho, S. L. *et al.* Sea surface temperature variability in the Pacific sector of the Southern Ocean over the past 700 kyr. *Paleoceanography* **27**, (2012).

48. Pichon, J.-J. *et al.* Surface water temperature changes in the high latitudes of the southern hemisphere over the Last Glacial-Interglacial Cycle. *Paleoceanography* **7**, 289–318 (1992).

49. Labeyrie, L. *et al.* Hydrographic changes of the Southern Ocean (southeast Indian Sector) Over the last 230 kyr. *Paleoceanography* **11**, 57–76 (1996).

50. Sicre, M. A. *et al.* Mid-latitude Southern Indian Ocean response to Northern Hemisphere Heinrich events. *Earth and Planetary Science Letters* **240**, 724–731 (2005).
51. Waelbroeck, C. *et al.* Constraints on the magnitude and patterns of ocean cooling at the Last Glacial Maximum. *Nature Geosci* **2**, 127–132 (2009).
52. Shakun, J. D. *et al.* Global warming preceded by increasing carbon dioxide concentrations during the last deglaciation. *Nature* **484**, 49–54 (2012).
53. Moore, J. K., Abbott, M. R. & Richman, J. G. Location and dynamics of the Antarctic Polar Front from satellite sea surface temperature data. *J. Geophys. Res.* **104**, 3059–3073 (1999).
54. Dong, S., Sprintall, J. & Gille, S. T. Location of the Antarctic Polar Front from AMSR-E Satellite Sea Surface Temperature Measurements. *Journal of Physical Oceanography* **36**, 2075–2089 (2006).
55. Belkin, I. M. & Gordon, A. L. Southern Ocean fronts from the Greenwich meridian to Tasmania. *Journal of Geophysical Research: Oceans* **101**, 3675–3696 (1996).
56. Park, Y.-H. *et al.* Polar Front around the Kerguelen Islands: An up-to-date determination and associated circulation of surface/subsurface waters. *Journal of Geophysical Research: Oceans* **119**, 6575–6592 (2014).
57. Carter, L. & Cortese, G. Change in the Southern Ocean: Responding to Antarctica. *PAGES news* **17**, 30–32 (2009).
58. Thöle, L. M. *et al.* Glacial-interglacial dust and export production records from the Southern Indian Ocean. *Earth and Planetary Science Letters* **525**, 115716 (2019).
59. Pauthenet, E. *et al.* Seasonal Meandering of the Polar Front Upstream of the Kerguelen Plateau. *Geophysical Research Letters* **45**, 9774–9781 (2018).

60. Marcott, S. A., Shakun, J. D., Clark, P. U. & Mix, A. C. A Reconstruction of Regional and Global Temperature for the Past 11,300 Years. *Science* (2013) doi:10.1126/science.1228026.

61. Shevenell, A. E., Ingalls, A. E., Domack, E. W. & Kelly, C. Holocene Southern Ocean surface temperature variability west of the Antarctic Peninsula. *Nature* **470**, 250–254 (2011).

62. Lu, J., Chen, G. & Frierson, D. M. W. The Position of the Midlatitude Storm Track and Eddy-Driven Westerlies in Aquaplanet AGCMs. *Journal of the Atmospheric Sciences* **67**, 3984–4000 (2010).

63. Timmermann, A. *et al.* Modeling Obliquity and CO2 Effects on Southern Hemisphere Climate during the Past 408 ka. *Journal of Climate* **27**, 1863–1875 (2014).

64. Studer, A. S. *et al.* Increased nutrient supply to the Southern Ocean during the Holocene and its implications for the pre-industrial atmospheric CO2 rise. *Nature Geosci* **11**, 756–760 (2018).

65. Jones, D. C., Ito, T. & Lovenduski, N. S. The transient response of the Southern Ocean pycnocline to changing atmospheric winds. *Geophysical Research Letters* **38**, (2011).

66. Kohfeld, K. E. & Chase, Z. Temporal evolution of mechanisms controlling ocean carbon uptake during the last glacial cycle. *Earth and Planetary Science Letters* **472**, 206–215 (2017).

67. Frierson, D. M. W., Lu, J. & Chen, G. Width of the Hadley cell in simple and comprehensive general circulation models. *Geophysical Research Letters* **34**, (2007).

68. Shakun, J. D., Lea, D. W., Lisiecki, L. E. & Raymo, M. E. An 800-kyr record of global surface ocean δ 18 O and implications for ice volume-temperature coupling. *Earth and Planetary Science Letters* **426**, 58–68 (2015).

69. Lee, S.-Y., Chiang, J. C. H., Matsumoto, K. & Tokos, K. S. Southern Ocean wind response to North Atlantic cooling and the rise in atmospheric CO_2: Modeling perspective and paleoceanographic implications. *Paleoceanography* **26**, PA1214 (2011).
70. Fletcher, M.-S. *et al.* Northward shift of the southern westerlies during the Antarctic Cold Reversal. *Quaternary Science Reviews* **271**, 107189 (2021).
71. Lee, S.-Y. & Poulsen, C. J. Obliquity and precessional forcing of continental snow fall and melt: implications for orbital forcing of Pleistocene ice ages. *Quaternary Science Reviews* **28**, 2663–2674 (2009).
72. Brayshaw, D. J., Hoskins, B. & Blackburn, M. The Storm-Track Response to Idealized SST Perturbations in an Aquaplanet GCM. *Journal of the Atmospheric Sciences* **65**, 2842–2860 (2008).
73. Nakamura, H., Sampe, T., Goto, A., Ohfuchi, W. & Xie, S.-P. On the importance of midlatitude oceanic frontal zones for the mean state and dominant variability in the tropospheric circulation. *Geophysical Research Letters* **35**, (2008).
74. Michel, C. & Rivière, G. Sensitivity of the Position and Variability of the Eddy-Driven Jet to Different SST Profiles in an Aquaplanet General Circulation Model. *Journal of the Atmospheric Sciences* **71**, 349–371 (2014).
75. Lund, D. C., Adkins, J. F. & Ferrari, R. Abyssal Atlantic circulation during the Last Glacial Maximum: Constraining the ratio between transport and vertical mixing. *Paleoceanography* **26**, (2011).
76. De Boer, A. M. & Hogg, A. McC. Control of the glacial carbon budget by topographically induced mixing. *Geophysical Research Letters* **41**, 4277–4284 (2014).
77. Bereiter, B. *et al.* Revision of the EPICA Dome C CO_2 record from 800 to 600 kyr before present: Analytical bias in the EDC CO2 record. *Geophys. Res. Lett.* **42**, 542–549 (2015).

78. Vimeux, F., Cuffey, K. M. & Jouzel, J. New insights into Southern Hemisphere temperature changes from Vostok ice cores using deuterium excess correction. *Earth and Planetary Science Letters* **203**, 829–843 (2002).
79. Graff, L. S. & LaCasce, J. H. Changes in the Extratropical Storm Tracks in Response to Changes in SST in an AGCM. *Journal of Climate* **25**, 1854–1870 (2012).
80. Hersbach, H. *et al.* The ERA5 global reanalysis. *Quarterly Journal of the Royal Meteorological Society* **146**, 1999–2049 (2020).
81. Bell, B. *et al.* The ERA5 global reanalysis: Preliminary extension to 1950. *Quarterly Journal of the Royal Meteorological Society* **147**, 4186–4227 (2021).
82. Berger, A. & Loutre, M. F. Insolation values for the climate of the last 10 million years. *Quaternary Science Reviews* **10**, 297–317 (1991).
83. Schouten, S., Hopmans, E. C. & Sinninghe Damsté, J. S. The organic geochemistry of glycerol dialkyl glycerol tetraether lipids: A review. *Organic Geochemistry* **54**, 19–61 (2013).
84. Auderset, A., Schmitt, M. & Martínez-García, A. Simultaneous extraction and chromatographic separation of n-alkanes and alkenones from glycerol dialkyl glycerol tetraethers via selective Accelerated Solvent Extraction. *Organic Geochemistry* **143**, 103979 (2020).
85. Hopmans, E. C., Schouten, S. & Sinninghe Damsté, J. S. The effect of improved chromatography on GDGT-based palaeoproxies. *Organic Geochemistry* **93**, 1–6 (2016).
86. Schouten, S. *et al.* An interlaboratory study of TEX86 and BIT analysis of sediments, extracts, and standard mixtures. *Geochemistry, Geophysics, Geosystems* **14**, 5263–5285 (2013).
87. Ho, S. L. *et al.* Appraisal of TEX86 and TEX86L thermometries in subpolar and polar regions. *Geochimica et Cosmochimica Acta* **131**, 213–226 (2014).

Supplementary Files

This is a list of supplementary files associated with this preprint. Click to download.

- 20220214SupplementaryInformation.pdf